Biochemical and Biophysical Research Communications 446 (2014) 965–970

Contents lists available at ScienceDirect

Biochemical and Biophysical Research Communications

journal homepage: www.elsevier.com/locate/ybbrc

Crystal structure and biochemical studies of *Brucella melitensis* 5′-methylthioadenosine/S-adenosylhomocysteine nucleosidase

Xusheng Kang [a,b], Yan Zhao [a], Daohua Jiang [a], Xuemei Li [a], Xianping Wang [a], Yan Wu [a,c], Zeliang Chen [d], Xuejun C. Zhang [a,*]

[a] National Laboratory of Biomacromolecules, Institute of Biophysics, Chinese Academy of Sciences, Beijing 100101, China
[b] University of Chinese Academy of Sciences, Beijing 100049, China
[c] Food Science and Engineering College, Beijing University of Agriculture, Beijing 102206, China
[d] Department of Infectious Disease Control, Institute of Disease Control and Prevention, Academy of Military Medical Sciences, Beijing 100071, China

ARTICLE INFO

Article history:
Received 7 March 2014
Available online 20 March 2014

Keywords:
Brucella
MTAN
Crystal structure

ABSTRACT

The prokaryotic 5′-methylthioadenosine/S-adenosylhomocysteine nucleosidase (MTAN) catalyzes the irreversible cleavage of the glycosidic bond in 5′-methylthioadenosine (MTA) and S-adenosylhomocysteine (SAH), a process that plays a key role in several metabolic pathways. Its absence in all mammalian species has implicated this enzyme as a promising target for antimicrobial drug design. Here, we report the crystal structure of *Bm*MTAN in complex with its product adenine at a resolution of 2.6 Å determined by single-wavelength anomalous dispersion method. 11 key residues were mutated for kinetic characterization. Mutations of Tyr134 and Met144 resulted in the largest overall increase in *Km*, whereas mutagenesis of residues Glu18, Glu145 and Asp168 completely abolished activity. Glu145 and Asp168 were identified as active site residues essential for catalysis. The catalytic mechanism and implications of this structure for broad-based antibiotic design are discussed.

1. Introduction

Brucellosis is a common zoonotic disease in the world that is caused by the Gram-negative bacterium Brucella. It has brought significant damage to both human's health and animal breeding. Currently used anti-Brucellosis drugs are likely to display limited efficacy, in particular with the emergence of MDR (multidrug-resistant) and XDR (extensively drug-resistant) strains of Brucella. Therefore, identifying new drug targets and understanding the underlying mechanisms of these targets are crucial for the development of new and effective anti-Brucellosis therapies.

5′-Methylthioadenosine/S-adenosylhomocysteine nucleosidase (MTAN) is a dual substrate-specific enzyme that irreversibly hydrolyzes the glycosidic bond of 5′-methylthioadenosine (MTA) or S-adenosylhomocysteine (SAH) to form adenine, together with either 5′-methylthioribose or S-ribosylhomocysteine [1]. It plays a key role in four metabolic processes: methylation of DNA and other macromolecules [2], polyamine biosynthesis [3,4], methionine recycling [5] and bacterial quorum sensing [6]. The absence of this nucleosidase in mammalian species, together with the fact that it is essential for the metabolism of MTA and SAH in many microbes, have made this enzyme a potential antibiotic target.

Previously, several *Escherichia coli* MTAN structures have been determined [7–10] and deposited in the Protein Data Bank. These include complexes with substrate and transition-state analogues as well as products, and they provide a strong foundation for structure-based inhibitor design. The structures of MTAN from the pathogenic bacterium *Staphylococcus aureus*, *Streptococcus pneumonia* and *Helicobacter pylori* have also been determined in complex with a transition-state analogue [11–13]. The analysis of these structures showed that their active sites can be divided into three separate regions, the purine, ribose, and 5′-alkylthio-binding subsites. The reactions catalyzed by MTAN are similar to those catalyzed by nucleoside phosphorylases (NP-1) [7,8]. Although the catalytic mechanism of the nucleoside phosphorylases has been studied in great detail, there are several features of the MTAN mechanism that appear to differ from the nucleoside phosphorylases and hydrolases that need to be examined.

Abbreviations: *Bm*MTAN, *Brucella melitensis* MTAN; INT, 2-(4-iodophenyl)-3-(4-nitrophenyl)-5-phenyltetrazolium chloride; MTA, 5′-methylthioadenosine; MTAN, MTA/SAH nucleosidase; NP-1, nucleoside phosphorylase-1; PDB, Protein Data Bank; PEG, polyethylene glycol; *r.m.s.d.*, root mean square deviation; SAD, single-wavelength anomalous diffraction; SAH, S-adenosylhomocysteine; SeMet, selenomethionine; WT, wild-type.

* Corresponding author.
E-mail address: zhangc@ibp.ac.cn (X.C. Zhang).

http://dx.doi.org/10.1016/j.bbrc.2014.03.045
0006-291X/

To determine whether the structure of the *E. coli* enzyme could be used as a template for broad-based antibiotic design, the structure of the nucleosidase from the pathogenic bacterium *Brucella melitensis* (*Bm*MTAN) in complex with its product adenine was analyzed. To further explore the catalytic mechanism of MTAN, we introduced single amino acid substitutions in the active site and examined the role of each residue. The results for the kinetic analysis allowed us to confirm the enzymatic mechanisms of the Brucella MTAN nucleosidase.

2. Materials and methods

2.1. Protein expression and purification

Seleno-methionine substituted *Bm*MTAN was expressed in the *E. coli* BL21(DE3) strain for 18 h at 16 °C from a pMCSG7-based vector. The harvested cell pellets were resuspended in 20 mM Tris–HCl (pH 8.2), 500 mM NaCl. Cells were disrupted using a High Pressure Breaking method (AVESTIN Company, EF-C3), and the lysate was centrifuged at 30,700*g* for 30 min at 4 °C to remove unbroken cells and debris. The supernatant was applied twice to a nickel affinity column (Qiagen), and then washed with 20 mM Tris–HCl (pH 8.2), 500 mM NaCl and 10 mM imidazole to remove proteins bound nonspecifically. The recombinant *Bm*MTAN was eluted with 20 mM Tris–HCl (pH 8.2), 500 mM NaCl and 500 mM imidazole. The target protein was further purified using a Superdex-200 gel filtration column (GE Healthcare). The buffer for gel filtration chromatography contained 20 mM Tris–HCl (pH 8.2), 100 mM NaCl and 10% (v/v) glycerol. 2 mM β-mercaptoethanol was added to all buffers to maintain reducing conditions for the seleno-methionine (SeMet) residues. Peak fractions were collected (monitored by 280 nm absorption) and concentrated to 30 mg/mL for crystallization.

2.2. Crystallization

Crystal screening experiments were first carried out at 16 °C using a Mosquito crystallization setting robot (TTP LabTech), with a "hanging-drop" vapor diffusion method by mixing 200 nL of protein solution (10 mg/mL in 20 mM Tris–HCl (pH 8.2), 100 mM NaCl and 10% glycerol) and 200 nL reservoir solution from commercial crystal screen kits. Crystals appeared a few days later in some conditions. Two conditions were optimized. The crystal used for data collection was grown in 20% (w/v) PEG-1000, 0.1 M phosphate–citrate (pH 4.2) and 0.2 M Li_2SO_4.

2.3. Data collection and structure determination

X-ray diffraction data were collected at 100 K on beamline BL41XU at SPring-8 synchrotron radiation facility (Japan). One data set of SeMet–*Bm*MTAN was collected at wavelength 0.9791 Å. Data processing for SeMet crystals was carried out using the HKL2000 program package [14]. The structure of SeMet–*Bm*MTAN was determined using single-wavelength anomalous diffraction (SAD) method. Fourteen of the sixteen expected selenium sites were located using the ShelxD program [15]. Phasing, model building and structure refinement were performed using the Phenix software suite [16]. The models were further refined manually using Coot software [17]. Data collection and refinement statistics are provided in Table 1. Secondary structures were defined using the DSSP program [18]. Structural figures were prepared using Pymol software [19].

2.4. Site-directed mutagenesis and kinetic characterization

The structure of *Bm*MTAN in complex with adenine allowed the identification of potential binding and catalytic residues in the purine, ribose, and 5′-alkylthio binding sites. Accordingly, residues Arg85, Tyr134, Ser167, and Asp168 in the purine binding site; Glu18, Met144, Glu145, and Arg164 in the ribose binding site; and Ala15, Val34, and Trp179 in the 5′-alkylthio binding site were targeted for mutagenesis. In designing these mutants, amino acid substitutions were kept as isosteric as possible to minimize any structural variations that may occur in the active site as a consequence. Mutants were generated by fusion PCR, using the native *Bm*MTAN expression plasmid as a template [20].

The catalytic activity of *Bm*MTAN was examined using a xanthine oxidase-coupled spectrophotometric assay [21]. Changes in absorption at 470 nm were converted to the amount of adenine released using a molar absorption coefficient of 15,400 M^{-1} cm^{-1} at pH 7.0. All reactions were performed in 100 mM HEPES (pH 7.5) using 10 nM–4 μM *Bm*MTAN, 0.28 units of xanthine oxidase (Sigma–Aldrich Chemicals) and 1 mM INT (Sigma–Aldrich Chemicals) in a final volume of 250 μL. The concentrations of MTA and SAH were varied from 0.6 to 100 μM. The $A_{470\ nm}$ of the reaction mixture was recorded every 10 min at 25 °C for 1 h using a 96-well plate reader (Thermo). Reactions without *Bm*MTAN were used as negative controls. Data for determining the kinetic constants were fitted to the Michaelis–Menten equation using GRAPHPAD PRISM v.5.0 (GraphPad Software).

2.5. Thermofluor-based stability verification

To estimate the stability of the recombinant mutant samples, we performed Thermofluor experiments using a 96-well qPCR instrument, Bio-Rad CFX96 (BioRad, US). Sypro Orange (Invitrogen, US) was used as a fluorescence probe, since it binds the hydrophobic amino acide residues as they become accessible during protein denaturation. Sypro Orange binding results in a fluorescence

Table 1
Data collection and refinement statistics.

Data	*Bm*MTAN-adenine (SeMet)
Data collection	
Space group	$P6_522$
Unit-cell parameters (Å)	a = 97.3, b = 97.3, c = 175.1, $\alpha = \beta$ = 90°, γ = 120°
Wavelength (Å)	0.97910
Resolution (Å)	50.0–2.60 (2.69–2.60)
R_{merge}[a] (%)	19.9 (85.1)
Completeness (%)	99.9 (99.6)
Redundancy	19.2 (14.9)
Average I/σ (I)	17.2 (3.0)
Observed reflections	300,476
Unique reflections	15,654 (1526)
Structure refinement	
Resolution (Å)	37.4–2.60
R_{work}[b]/R_{free}[c] (%)	22.2/26.0
No. of non-hydrogen atoms	
Mean B factor (Å^2)	
Protein	21.7
Ligand	20.0
Water	15.5
r.m.s.d. from ideal	
Bond length (Å)	0.004
Bond angles (°)	0.961
Ramachandran plot (%)	
Favored region	95.6
Allowed region	4.4
Disallowed region	0

Values in parentheses indicate the highest-resolution shell.
[a] $R_{merge} = \Sigma_{hkl}\Sigma_i|I(hkl)_i - \langle I(hkl)\rangle|/\Sigma_{hkl}\Sigma_i\ I(hkl)_i$.
[b] $R_{work} = \Sigma_{hkl}\ |\mathrm{Fo}(hkl) - \mathrm{Fc}(hkl)|/\Sigma_{hkl}\mathrm{Fo}(hkl)$.
[c] R_{free} was calculated for a test set of reflections (5%) omitted from the refinement.

signal, with an excitation maximum at 488 nm and an emission maximum at 580 nm. The volume of each sample was 20 μL, and the final concentration of the protein was 0.3 μg/μL. Protein samples were typically diluted at a 1:20 ratio from an original stock into HEPES buffer (100 mM HEPES, pH 7.5) containing the either substrate MTA or SAH at 0.35, 1.75, 5.25 mM or 0.5, 2.5, 7.5 mM, respectively. The qPCR instrument was programmed to increase temperature from 25 to 95 °C at a rate of 1 °C/min. The melting temperature, T_m corresponded to the minimum of the first derivative of the denaturation curve.

3. Results and discussion

3.1. Overview of BmMTAN structure

*Bm*MTAN, comprised of 209 amino acid residues, was over-expressed in *E. coli* as a recombinant protein fused with an N-terminal His_8-tag to facilitate purification, with an overall calculated molecular weight of 25 kDa. The crystal structure of the *Bm*MTAN was determined using the SeMet-based single-wavelength anomalous diffraction (SAD) method, and was refined to 2.6 Å resolution, with R-work and R-free values of 22.2% and 26.0%, respectively. The crystal form of *Bm*MTAN belongs to space group $P6_522$, with unit cell parameters $a = 97.3$ Å, $b = 97.3$ Å, $c = 175.1$ Å (Table 1). According to Matthews coefficient analysis, there are two molecules in one asymmetric unit, at a solvent content of 46% ($V_M = 2.3$ Å^3/Da). The interface of the two monomers is highly hydrophobic. Each monomer consists of a mixed α/β domain, with a central mixed eight-stranded β-sheet flanked by five α-helices (Fig. 1A and B). The total interface area between the two monomers is 1390 Å^2, and comprises 14% of the surface of each monomer.

3.2. Active sites of BmMTAN structure

An unambiguous electron density was observed in the active site of *Bm*MTAN throughout the refinement process. In the late stages of refinement, this density was clearly identified as an adenine molecule (Fig. 1A and C), despite the fact that *Bm*MTAN crystals were obtained in the absence of adenine in both media and buffers. The adenine was shown to establish several hydrogen bonds to the peptide main chain. The position of this adenine superimposes almost perfectly with the adenine ring of the substrate analog FMA in the *Ec*MTAN structure (1NC3) [10], which allowed for identification of residues involved in substrate binding. The active site of MTAN enzyme is typically described in terms of three subsites, which accommodate the adenine, ribose and 5′-alkylthio moieties of the substrate. Modeling FMA into the active site putatively identified the residues involved in the three subsites. The adenine-binding site in *Bm*MTAN involves the loop between β strand β_6 and β_7, together with the loop between β strand β_8 and α helix α_5. This site is composed of the residues Tyr134, Glu135, Ser167 and Asp168 (Fig. 2A). The phenyl ring of Tyr134 makes a nearly perpendicular herringbone interaction with the adenine ring. Additional potential interactions exist between $O_\delta1$ and $O_\delta2$ of Asp168 and the N7 and the N6 amido group on the adenine ring, respectively. Asp168 is stabilized by two hydrogen bonds from Ser167 O_γ and the amide N atom of Ala170. In the present structure, these interactions are too long for the formation of hydrogen bonds, but a conformational change may occur upon substrate binding that could bring the aspartic acid closer to N7. The values of the *B* factors in this region are higher than those for other residues in β_8 and α_5, suggesting that these residues are fairly dynamic and conformationally flexible. According to the structure of *Ec*MTAN in complex with its substrate analog FMA

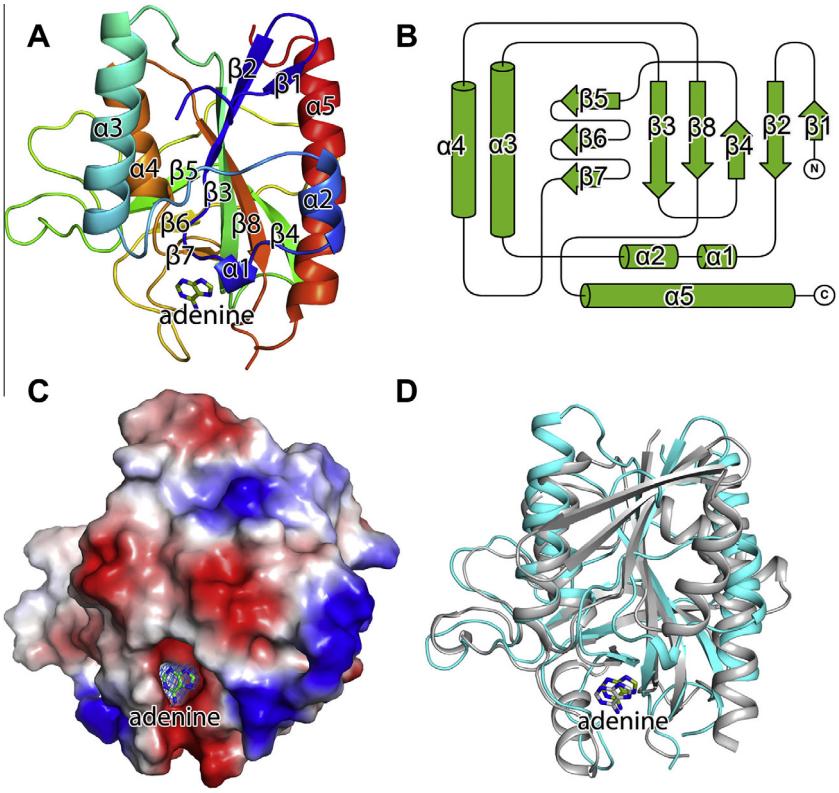

Fig. 1. Overall structure of *Bm*MTAN. (A) Ribbon and surface representations of *Bm*MTAN. (B) Topology diagram of *Bm*MTAN. (C) Electrostatic potential surface of *Bm*MTAN. Positively charged regions, negatively charged regions, and neutral zones are presented in blue, red and white, respectively. (D) Structure superposition of *Bm*MTAN (cyan) and *Ec*MTAN (gray).

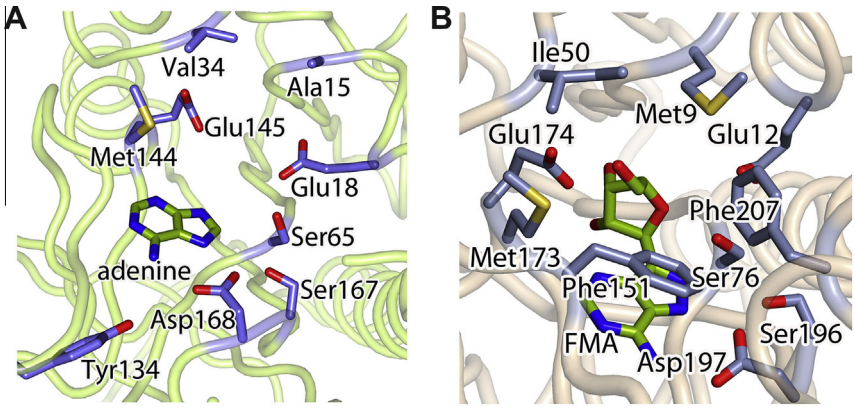

Fig. 2. Active sites in *Bm*MTAN and *Ec*MTAN. (A) The active site of *Bm*MTAN in complex with its product adenine. (B) The active site of *Ec*MTAN in complex with the substrate analog (FMA).

(Fig. 2B), residues Glu18, Ser65, Met144 and Glu145 of *Bm*MTAN lie on the surface of the ribose-binding subsite, residues Ala15, Val34, and Trp179 interact with the 5′-alkylthio moiety (Fig. 2A).

3.3. Stability and kinetic characterization of BmMTAN mutants

To study the stability of *Bm*MTAN mutants, we performed a thermofluor analysis with or without the substrate MTA/SAH (three concentrations) (Table S1).

Without the substrate MTA/SAH, the T_m values of most *Bm*MTAN mutants were 2–9 degrees lower compared to WT, and the T_m values of Y134F, S167A, D168A and D168N were the same as WT. With the substrate MTA/SAH, the T_m values of all mutants as well as the WT were higher than those samples lacking the substrate. In addition, the higher the concentrations of the substrate MTA/SAH, the higher the increase of the T_m values. Moreover, the T_m values of the mutants increased more when in complex with MTA, relative to those observed for SAH complexes. Of the *Bm*MTAN mutants in complex with equal ratios of MTA/SAH, the T_m values of most mutants were 4–15 degrees lower compared to WT, except for mutant Y134F, which was found to be nearly the same as WT. Noteworthy are the mutants D168A and D168N, for which the T_m values were 12 and 21 degrees higher, respectively, relative to WT upon use of equal amounts of MTA. For each SAH concentration tested, the T_m values of the mutant D168N were 4–11 degrees higher compared to the corresponding WT sample (see Table S1).

To investigate the functional consequences of our mutations, the activities of WT and mutant *Bm*MTAN were quantified spectrophotometrically by monitoring the production of formazan at 470 nm [21]. All mutant kinetics were measured at the pH optima (pH = 7.5). All active enzymes displayed classic kinetics, and the initial velocity data were fit to the Michaelis–Menten equation to determine the kinetic parameters using GRAPHPAD PRISM v.5.0 (GraphPad Software), with K_m and V_{max}. The value of k_{cat} was calculated using V_{max}.

Both WT and mutants were assayed using the two natural substrates, MTA and SAH, across a range of substrate concentration from 0.6 to 100 μM (Tables 2–4). WT *Bm*MTAN showed k_{cat}/K_m values of $(4.0 \pm 0.8) \times 10^6\ s^{-1}\ M^{-1}$ and $(1.8 \pm 0.4) \times 10^6\ s^{-1}\ M^{-1}$ for MTA and SAH, respectively. The K_m values measured for MTA and SAH were consistent with previously reported values [22]. Of the four residues mutated in the purine-binding site, the largest kinetic effect was observed for mutations of Asp168 (Table 2). The D168A and D168N mutants were completely inactive. Proteins with mutations at their Arg85, Tyr134 and Ser167 sites retained ~7%, 0.6% and ~4% of their catalytic efficiency relative to WT, respectively. Mutations to Tyr134 exhibited a larger change in K_m than k_{cat}. Of the four residues mutated in the ribose-binding site, substitutions at Glu18 and Glu145 completely abolished activity (Table 3). M144A exhibited <1% catalytic efficiency compared to WT, with a larger change in K_m than k_{cat}. The R164A variant displayed catalytic efficiencies of ~17% for both MTA and SAH. Mutations at the 5′-alkylthio binding site, i.e. Ala15, Val34 and Trp179, retained their respective catalytic efficiencies at levels of ~15%, ~16% and ~3% when compared to WT (Table 4).

3.4. Substrate preference of BmMTAN

Despite extensive structural and biochemical studies, the molecular mechanisms of substrate specificity for MTAN remain to be elucidated. Our kinetic characterization of *Bm*MTAN revealed that *Bm*MTAN possesses comparable efficiencies for hydrolyzing MTA and SAH, however, it also displays a preference for MTA hydrolysis, as judged by our K_m and k_{cat}/K_m measurements. These results were consistent with previous reports investigating other bacterial MTANs [12,22]. The *Bm*MTAN mutant D168N bound tighter to the substrate MTA than SAH, as indicated by the values of both melting temperature (T_m) (Table S1) and dissociation constant (K_d), determined in an ITC experiment using *Bm*MTAN mutants (data not shown). This suggests that the catalytic efficiency of *Bm*MTAN is determined largely by the binding capacity to the substrate, however, this conclusion may not be entirely correct. It is known that bacterial MTANs exhibit comparable efficiencies in hydrolyzing MTA and SAH, whereas plant enzymes were evolutionarily selected with a preference for MTA, with either no or significantly reduced activity towards SAH [23]. Earlier investigations using the ITC method indicated that, whilst *Arabidopsis thaliana* *At*MTAN1 can bind SAH, it cannot hydrolyze this substrate. The lack of catalytic activity appears to be related to the enzyme's inability to bind the substrate in a catalytically competent manner [24]. Homology modeling analysis indicates that Phe148/Phe120 of *Burkholderia thailandensis* MTAN may hinder the divergence in specificity of the enzyme, and thus could be responsible for the low activity of MTAN for SAH [25]. Alternatively, the side-chain of the SAH is longer than MTA, and may therefore affect the binding of SAH to the *Bm*MTAN.

3.5. Catalytic mechanism of BmMTAN

Previously determined structures of MTAN revealed strong similarities in the overall structure and active site architecture to the nucleoside phosphorylase-1 family [7,8], which led us to propose that MTAN shares a similar catalytic mechanism with the NP-1

Table 2
Kinetic parameters for purine binding subsite mutants.

Enzyme	Substrate	K_m (μM)	K_{cat} (s^{-1})	k_{cat}/K_m (s^{-1} M^{-1})	Catalytic efficiency (%)
WT	MTA	2.2 ± 0.2	8.8 ± 0.3	$(4.0 \pm 0.8) \times 10^6$	100
	SAH	4.0 ± 0.2	7.1 ± 0.2	$(1.8 \pm 0.4) \times 10^6$	100
R85A	MTA	5.4 ± 0.2	1.4 ± 0.3	$(2.5 \pm 0.1) \times 10^5$	6.3
	SAH	6.8 ± 0.3	$(9.3 \pm 0.3) \times 10^{-1}$	$(1.4 \pm 0.1) \times 10^5$	7.6
R85H	MTA	4.8 ± 0.2	1.3 ± 0.2	$(2.8 \pm 0.2) \times 10^5$	7.1
	SAH	6.1 ± 0.3	$(9.2 \pm 0.2) \times 10^{-1}$	$(1.5 \pm 0.1) \times 10^5$	8.1
Y134A	MTA	28.0 ± 2.0	$(7.8 \pm 0.3) \times 10^{-1}$	$(2.8 \pm 0.3) \times 10^4$	0.7
	SAH	38.1 ± 4.1	$(3.9 \pm 0.2) \times 10^{-1}$	$(1.0 \pm 0.2) \times 10^4$	0.6
Y134F	MTA	30.1 ± 2.1	$(7.1 \pm 0.4) \times 10^{-1}$	$(2.4 \pm 0.6) \times 10^4$	0.6
	SAH	45.2 ± 4.2	$(3.5 \pm 0.3) \times 10^{-1}$	$(7.8 \pm 2.2) \times 10^3$	0.4
S167A	MTA	4.4 ± 0.2	$(5.8 \pm 0.3) \times 10^{-1}$	$(1.3 \pm 0.1) \times 10^5$	3.3
	SAH	5.6 ± 0.3	$(5.5 \pm 0.2) \times 10^{-1}$	$(1.0 \pm 0.1) \times 10^5$	5.6
D168A	MTA		Inactive		
	SAH		Inactive		
D168N	MTA		Inactive		
	SAH		Inactive		

Table 3
Kinetic parameters for ribose binding subsite mutants.

Enzyme	Substrate	K_m (μM)	K_{cat} (s^{-1})	k_{cat}/K_m (s^{-1} M^{-1})	Catalytic efficiency (%)
WT	MTA	2.2 ± 0.2	8.8 ± 0.3	$(4.0 \pm 0.8) \times 10^6$	100
	SAH	4.0 ± 0.2	7.1 ± 0.2	$(1.8 \pm 0.4) \times 10^6$	100
E18A	MTA		Inactive		
	SAH		Inactive		
E18Q	MTA		Inactive		
	SAH		Inactive		
M144A	MTA	35.1 ± 3.2	$(5.1 \pm 0.4) \times 10^{-1}$	$(1.5 \pm 0.2) \times 10^4$	0.4
	SAH	95.1 ± 8.2	$(1.5 \pm 0.3) \times 10^{-1}$	$(1.6 \pm 0.5) \times 10^3$	0.1
E145A	MTA		Inactive		
	SAH		Inactive		
E145Q	MTA		Inactive		
	SAH		Inactive		
R164A	MTA	8.0 ± 0.34	8.0 ± 0.3	$(6.0 \pm 0.5) \times 10^5$	15.0
	SAH	13.3 ± 0.9	4.7 ± 0.2	$(3.5 \pm 0.4) \times 10^5$	19.4

Table 4
Kinetic parameters for 5′-alkylthio binding subsite mutants.

Enzyme	Substrate	K_m (μM)	K_{cat} (s^{-1})	k_{cat}/K_m (s^{-1} M^{-1})	Catalytic efficiency (%)
WT	MTA	2.2 ± 0.2	8.8 ± 0.3	$(4.0 \pm 0.8) \times 10^6$	100
	SAH	4.0 ± 0.2	7.1 ± 0.2	$(1.8 \pm 0.4) \times 10^6$	100
A15M	MTA	3.1 ± 0.2	1.8 ± 0.1	$(5.8 \pm 0.5) \times 10^5$	14.5
	SAH	4.1 ± 0.2	1.1 ± 0.1	$(2.7 \pm 0.3) \times 10^5$	15.2
V34A	MTA	5.3 ± 0.3	2.7 ± 0.2	$(5.1 \pm 0.4) \times 10^5$	12.5
	SAH	6.2 ± 0.3	2.1 ± 0.2	$(3.3 \pm 0.3) \times 10^5$	18.5
V34I	MTA	4.5 ± 0.2	2.5 ± 0.2	$(5.6 \pm 0.4) \times 10^5$	13.9
	SAH	5.8 ± 0.3	2.3 ± 0.2	$(3.9 \pm 0.3) \times 10^5$	21.5
W179A	MTA	5.4 ± 0.2	$(6.9 \pm 0.4) \times 10^{-1}$	$(1.3 \pm 0.1) \times 10^5$	3.3
	SAH	7.6 ± 0.4	$(8.6 \pm 0.2) \times 10^{-1}$	$(1.1 \pm 0.1) \times 10^5$	6.3
W179F	MTA	7.4 ± 0.3	$(5.8 \pm 0.4) \times 10^{-1}$	$(7.9 \pm 0.8) \times 10^4$	2.0
	SAH	9.8 ± 0.4	$(3.7 \pm 0.2) \times 10^{-1}$	$(3.8 \pm 0.3) \times 10^4$	2.1

family of enzymes [7]. NP-1 enzymes are generally thought to proceed through a two-step dissociative S_N1-type mechanism [26–28]. We therefore propose a similar catalytic mechanism for *Bm*MTAN. The first step involves proton donation occurs from the catalytic acid Asp168 to the N7 adenine to allow the formation of a hydrogen bond. The electron withdrawing purine base is stabilized by a flow of electrons from the ribose. This leads to ribosidic bond elongation, formation of the oxacarbenium-like ion, and partial positive charge buildup on the O3′, C3′, C2′, and C1′atoms. Following the formation of the oxacarbenium-like ion, at the transition state, the leaving group is removed and the oxacarbenium-like intermediate is stabilized by the nucleophilic water and Glu145. A Glu18-activated nucleophilic water attacks the anomeric carbon of the oxacarbenium intermediate to form the two products.

Our structure of *B. melitensis* MTAN described here reveals that the architecture of its active site and the nucleoside–enzyme interactions are identical to those found in its *E. coli* homologue (Fig. 1D). In addition, the enzyme structures determined for both *S. pneumonia* and *S. aureus* also show structural similarities to that of the *E. coli* homologue [12,13]. Furthermore, an alignment of available primary MTAN sequences from various bacterial pathogens demonstrated a degree of sequence identity that ranged from 30% to 100% (Fig. S1), with almost all active-site residues being conserved. The structural similarities observed suggest that any

of the available structures could be used for modeling or docking studies for the design of broad-spectrum antibiotics.

4. Deposition of coordinates

The coordinates for the structure have been deposited into the Protein Data Bank, with the ID 4PR3.

Acknowledgments

The authors thank Ya Wang, Yi Han, and other staff members of the Structural Biology Core Facility in the Institute of Biophysics, Chinese Academy of Sciences (CAS) for excellent technical assistance. This work was supported by a grant from the National Natural Science Foundation of China (Grant No. NSFC31200560).

Appendix A. Supplementary data

Supplementary data associated with this article can be found, in the online version, at http://dx.doi.org/10.1016/j.bbrc.2014.03.045.

References

[1] J.A. Duerre, A hydrolytic nucleosidase acting on S-adenosylhomocysteine and on 5′-methylthioadenosine, J. Biol. Chem. 237 (1962) 3737–3741.
[2] J.W. Miller, M.R. Nadeau, J. Smith, D. Smith, J. Selhub, Folate-deficiency-induced homocysteinaemia in rats: disruption of S-adenosylmethionine's co-ordinate regulation of homocysteine metabolism, Biochem. J. 298 (1994) 415–419.
[3] A. Raina, K. Tuomi, R.L. Pajula, Inhibition of the synthesis of polyamines and macromolecules by 5′-methylthioadenosine and 5′-alkylthiotubercidins in BHK21 cells, Biochem. J. 204 (1982) 697–703.
[4] R.L. Pajula, A. Raina, Methylthioadenosine, a potent inhibitor of spermine synthase from bovine brain, FEBS Lett. 99 (1979) 343–345.
[5] M.K. Riscoe, A.J. Ferro, J.H. Fitchen, Methionine recycling as a target for antiprotozoal drug development, Parasitol. Today 5 (1989) 330–333.
[6] X. Chen, S. Schauder, N. Potier, A. Van Dorsselaer, I. Pelczer, B.L. Bassler, F.M. Hughson, Structural identification of a bacterial quorum-sensing signal containing boron, Nature 415 (2002) 545–549.
[7] J.E. Lee, K.A. Cornell, M.K. Riscoe, P.L. Howell, Structure of *E. coli* 5′-methylthioadenosine/S-adenosylhomocysteine nucleosidase reveals similarity to the purine nucleoside phosphorylases, Structure 9 (2001) 941–953.
[8] J.E. Lee, K.A. Cornell, M.K. Riscoe, P.L. Howell, Structure of *Escherichia coli* 5′-methylthioadenosine/S-adenosylhomocysteine nucleosidase inhibitor complexes provide insight into the conformational changes required for substrate binding and catalysis, J. Biol. Chem. 278 (2003) 8761–8770.
[9] J.E. Lee, V. Singh, G.B. Evans, P.C. Tyler, R.H. Furneaux, K.A. Cornell, M.K. Riscoe, V.L. Schramm, P.L. Howell, Structural rationale for the affinity of pico- and femtomolar transition state analogues of *Escherichia coli* 5′-methylthioadenosine/S-adenosylhomocysteine nucleosidase, J. Biol. Chem. 280 (2005) 18274–18282.
[10] J.E. Lee, G.D. Smith, C. Horvatin, D.J. Huang, K.A. Cornell, M.K. Riscoe, P.L. Howell, Structural snapshots of MTA/AdoHcy nucleosidase along the reaction coordinate provide insights into enzyme and nucleoside flexibility during catalysis, J. Mol. Biol. 352 (2005) 559–574.
[11] D.R. Ronning, N.M. Iacopelli, V. Mishra, Enzyme–ligand interactions that drive active site rearrangements in the *Helicobacter pylori* 5′-methylthioadenosine/S-adenosylhomocysteine nucleosidase, Protein Sci. 19 (2010) 2498–2510.
[12] K.K. Siu, J.E. Lee, G.D. Smith, C. Horvatin-Mrakovcic, P.L. Howell, Structure of *Staphylococcus aureus* 5′-methylthioadenosine/S-adenosylhomocysteine nucleosidase, Acta Crystallogr. Sect. F Struct. Biol. Cryst. Commun. 64 (2008) 343–350.
[13] V. Singh, W. Shi, S.C. Almo, G.B. Evans, R.H. Furneaux, P.C. Tyler, G.F. Painter, D.H. Lenz, S. Mee, R. Zheng, V.L. Schramm, Structure and inhibition of a quorum sensing target from *Streptococcus pneumoniae*, Biochemistry 45 (2006) 12929–12941.
[14] Z. Otwinowski, W. Minor, Processing of X-ray diffraction data collected in oscillation mode, Methods Enzymol. 276 (1997) 307–326.
[15] T.R. Schneider, G.M. Sheldrick, Substructure solution with SHELXD, Acta Crystallogr. D Biol. Crystallogr. 58 (2002) 1772–1779.
[16] N. Echols, R.W. Grosse-Kunstleve, P.V. Afonine, G. Bunkoczi, V.B. Chen, J.J. Headd, A.J. McCoy, N.W. Moriarty, R.J. Read, D.C. Richardson, J.S. Richardson, T.C. Terwilliger, P.D. Adams, Graphical tools for macromolecular crystallography in PHENIX, J. Appl. Crystallogr. 45 (2012) 581–586.
[17] P. Emsley, K. Cowtan, Coot: model-building tools for molecular graphics, Acta Crystallogr. D Biol. Crystallogr. 60 (2004) 2126–2132.
[18] W. Kabsch, C. Sander, Dictionary of protein secondary structure: pattern recognition of hydrogen-bonded and geometrical features, Biopolymers 22 (1983) 2577–2637.
[19] L. Schrodinger, The PyMOL molecular graphics system, Version 1.3r1 (2010).
[20] R.C. Davidson, J.R. Blankenship, P.R. Kraus, M. de Jesus Berrios, C.M. Hull, C. D'Souza, P. Wang, J. Heitman, PCR-based strategy to generate integrative targeting alleles with large regions of homology, Microbiology 148 (2002) 2607–2615.
[21] S.M. Dunn, J.A. Bryant, M.W. Kerr, A simple spectrophotometric assay for plant 5′-deoxy-5′-methylthioadenosine nucleosidase using xanthine-oxidase as a coupling enzyme, Phytochem. Anal. 5 (1994) 286–290.
[22] J.E. Lee, W. Luong, D.J. Huang, K.A. Cornell, M.K. Riscoe, P.L. Howell, Mutational analysis of a nucleosidase involved in quorum-sensing autoinducer-2 biosynthesis, Biochemistry 44 (2005) 11049–11057.
[23] K.K. Siu, J.E. Lee, J.R. Sufrin, B.A. Moffatt, M. McMillan, K.A. Cornell, C. Isom, P.L. Howell, Molecular determinants of substrate specificity in plant 5′-methylthioadenosine nucleosidases, J. Mol. Biol. 378 (2008) 112–128.
[24] K.K. Siu, K. Asmus, A.N. Zhang, C. Horvatin, S. Li, T. Liu, B. Moffatt, V.L. Woods Jr., P.L. Howell, Mechanism of substrate specificity in 5′-methylthioadenosine/S-adenosylhomocysteine nucleosidases, J. Struct. Biol. 173 (2011) 86–98.
[25] Q. Gao, D. Zheng, Z. Yuan, Substrate preference of 5′-methylthioadenosine/S-adenosylhomocysteine nucleosidase in *Burkholderia thailandensis*, FEMS Microbiol. Lett. 339 (2013) 110–116.
[26] M.D. Erion, K. Takabayashi, H.B. Smith, J. Kessi, S. Wagner, S. Honger, S.L. Shames, S.E. Ealick, Purine nucleoside phosphorylase. 1. Structure–function studies, Biochemistry 36 (1997) 11725–11734.
[27] M.D. Erion, J.D. Stoeckler, W.C. Guida, R.L. Walter, S.E. Ealick, Purine nucleoside phosphorylase. 2. Catalytic mechanism, Biochemistry 36 (1997) 11735–11748.
[28] A. Fedorov, W. Shi, G. Kicska, E. Fedorov, P.C. Tyler, R.H. Furneaux, J.C. Hanson, G.J. Gainsford, J.Z. Larese, V.L. Schramm, S.C. Almo, Transition state structure of purine nucleoside phosphorylase and principles of atomic motion in enzymatic catalysis, Biochemistry 40 (2001) 853–860.